ELSEVIER

Chemical Engineering Journal 130 (2007) 79–85

Chemical Engineering Journal

www.elsevier.com/locate/cej

Mapping the 3D water dynamics in heterogeneous sands using thermal neutrons☆

A. Kaestner[a,*], R. Hassanein[b], P. Vontobel[b], P. Lehmann[a], J. Schaap[a], E. Lehmann[b], H. Flühler[a]

[a] *Institute of Terrestrial Ecosystems, ETH Zürich, Universitätstrasse 16, CH-8092 Zürich, Switzerland*
[b] *Paul Scherrer Institute, CH-5232 Villigen PSI, Switzerland*

Abstract

The transport of dissolved pollutants and nutrients in soils depends on the spatial and temporal distribution of soil water. The water flow is strongly affected by the presence of air and the heterogeneity of the soil structure. To investigate the influence of structures and air on the soil water dynamics, the distribution of water in a sand column was tomographed using thermal neutrons. The experiment was conducted using a column filled with $5 \times 5 \times 6$ sand cubes of 1 cm size. Each sand cube was filled with coarse or fine sand material. The volume fraction of the cubes filled with coarse sand was 33%. The cubes were arranged randomly. In the sample realization, a continuous path between top and bottom of the column within the coarse material existed. The continuity of this sand structure is expected to affect the water dynamics. At the beginning of the experiment, the pore space in the column was filled with water. Then, the column was drained by the application of a continuously changing suction force at the bottom of the column. After an equilibration period, the suction was released and water flowed back in the column. The water content in the sand cubes was mapped in intervals of one and a half minutes. A total tomography of the column was carried out in 53 s using an optimized flat panel. To increase the sensitivity of the thermal neutron tomography measurements, a mixture of normal water and heavy water was used. The drainage of the coarse sand was much faster than for the fine sand because the capillary forces are smaller and the hydraulic conductivity is high.

Keywords: Tomography; Flow visualization; Thermal neutrons; Image analysis; Porous media; Water dynamics

1. Introduction

The spatial and temporal distribution of soil water is of crucial importance for plant growth, availability of nutrients and concentration of dissolved pollutants. In addition, the water content determines the flow velocity of water and the transport of solutes. With decreasing water saturation, the water flow is reduced dramatically. The water dynamics can be modelled by determining the water distribution as a function of space and time. But the physics of these models is simplified and most often is only the water phase modelled. These models are based on material functions as the relationship between water content, water pressure and the hydraulic conductivity of the porous media. The principles of these material functions are given below. For more information, we refer to soil physics literature, e.g. Jury and Horton [1]. The dependency of the water content on the water pressure is given by the capillary forces. They are inversely proportional to the radius of a pore. The size of the pores also affects the water flow. Due to the friction at the solid walls, the water flow velocity increases with distance from the particles. The water flow velocity and water flow increases with increasing pore sizes. A fraction of pores may be drained for a certain pressure while water still remains in the smallest pores with the highest friction. Due to that, the water flow decreases non-linearly with decreasing water content. For a certain water pressure, the amount of retained water and the water flow must be determined. The determination of these material functions is very time consuming and is highly dependent on the maximum water content in the sample. Additionally, the material functions depend on the preceding drainage and wetting processes. This phenomenon is denoted as hysteresis and its effect on water dynamics has been shown in laboratory and field experiments (Wildenschild and Jensen [2], Lehmann et al. [3], and Schultze et al. [4]).

The water distribution can be measured by means of tomographic methods to avoid the uncertainties of the parameterized material functions and the simplified physics. We used thermal

☆ Expanded version of a talk presented at the Fourth World Congress on Industrial Process Tomography (Aizu, Japan, September 2005).

* Corresponding author.
E-mail addresses: anders.kaestner@env.ethz.ch (A. Kaestner), eberhard.lehmann@psi.ch (E. Lehmann).

1385-8947/$ – see front matter © 2006 Elsevier B.V. All rights reserved.
doi:10.1016/j.cej.2006.06.013

neutrons to measure the spatial and temporal water distribution and to relate the water dynamics to the structural properties of the medium.

At the pore scale, water distribution is determined by the size and the connectivity of the pore space. Water is retained in small pores with high capillary forces. Depending on the connectivity of the pore space, may also large pores remain water filled. This happens when the large pore is surrounded by small ones. Such effects of structure connectivity can also be found at larger scales. In this study, we analyzed the spatial and temporal water distribution in a sand column containing two different sand materials. The coarse sand material formed a continuous path between top and bottom of the column. The hydraulic properties of the two materials were determined in the laboratory [5]. Compared to the fine material, the hydraulic conductivity in the coarse sand was higher (370%) and the air-entry value was reduced (50%). So, in case of a drainage process, air can easily replace the water in the coarse sand because the capillary forces are small and the water outflow is fast. Reversely, for the wetting process, we expected that the capillary rise in the small pores of the fine sand is the dominant factor.

2. Samples and measurements

2.1. Sample description

To study the water dynamics in heterogeneous sand structures we prepared a rectangular sample column, containing an arrangement of $5 \times 5 \times 6$ sand cubes. The sand cubes had the dimensions $1\,\text{cm} \times 1\,\text{cm} \times 0.7\,\text{cm}$. The sample container was made of aluminum to reduce the neutron scattering and the beam attenuation by the container. The content of each sand cube was either fine quartz sand with particle sizes in the interval 100–500 μm or coarse sand, with particle sizes from 300 to 900 μm. The fraction of coarse-grained sand cubes represented 33% of the total amount of cubes in the sample column. The cube arrangement was determined by choosing the arrangement with the highest hydraulic conductivity out of a thousand numerical water flow simulations on randomized structures. Characteristic for the structure was that the coarser sand cubes formed a continuous path from top to bottom. The structure was heterogeneous on a macroscopic scale. The resulting structure is shown in Fig. 1a. For the evaluation of the experiment we introduce an

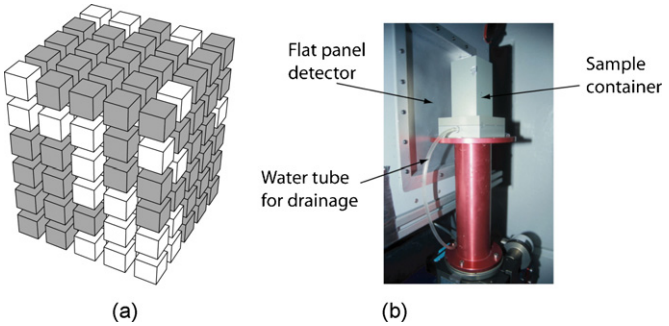

Fig. 1. Arrangement of coarse sand cubes in the sample (a) and a photograph of the sample and tomography setup (b).

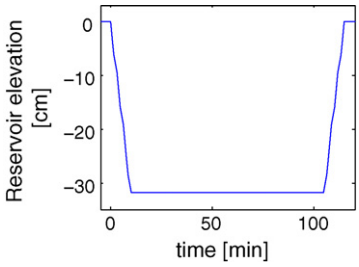

Fig. 2. The level in a water reservoir controls the drainage and wetting of the sand sample. The line gives the elevation of the reservoir watertable relative to the lower sample boundary.

indicator variable S_{material} that describes the arrangement of fine and coarse sand in the sample. After the packing, the structure was saturated with water. Then, a suction was applied at the bottom of the column to drain the sample. After an equilibration period, the column was wetted again. The whole process was scanned using thermal neutrons. In advance, the same drainage and wetting process was analyzed in the laboratory to relate the gray values in the measured images to a volumetric water content.

2.2. Source and sensors

The measurements were performed at the NEUTRA[1] beam line at the Paul Scherrer Institute, Switzerland. This beam line provides images using a beam of thermal neutrons as illuminating source (Lehmann et al. [6]). The radiographies used to reconstruct the tomographic images were acquired using thermal neutrons with an approximated Maxwell spectrum around 23.8 meV. The sensor was a ^{6}LiF doped ZnS scintillator with 250 μm thickness. The projections were captured using an amorphous Si flat panel. The nominal resolution was 127 μm/voxel. The images were reconstructed from 201 projections in 180 degrees. A set of 201 projections with a field of view of 97 mm × 122 mm was acquired within 53 s at a neutron flux level of about 4.6×10^6 n/cm^2/s.

2.3. Measurement sequence

In the initial state of the column was the reservoir watertable 1.4 cm above the lower boundary of the sand structure. The sample was completely saturated due to the capillary forces of the sand material. A mixture of 75% heavy water (D_2O) and 25% normal water (H_2O) was used in the experiment since it gave the best sensitivity for our measurements according to preliminary experiments. A mixture was used because 5 cm of normal water attenuates more than 99% of the beam intensity. This makes imaging with short exposure times impossible. The structure was drained and wetted by changing the water pressure at the bottom of the column as shown in Fig. 2. A suction force was applied to drain the sample, until the equilibrium for the given force was reached. Finally, the suction was released and water flowed back into the sample. Hence this experiment resulted in

[1] Homepage August 2006, http://neutra.web.psi.ch.

a drying step and a wetting step. The capture rate during the dynamic part of the experiment was one frame (3D) per 1.5 min, while the frame rate in the equilibration part was reduced to a small number of verification frames during a time of up to 2 h. The suction changed from minimum to maximum position within 10 min. We did not intend to change the pressure too fast, because the water volume during a complete scan should not change too much. Fast water content changes are not desired since the projection information will then change considerably between the first projection and the last one of the same scan sequence. This will in turn affect the reconstruction quality of volume images.

3. Image analysis

The measurements resulted in a large set of projection data that had to be converted into time sequences of volume images showing the water distribution in the samples. The processing of the data involved the correction of neutron scattering, beam hardening, and energy sensitivity of the detector followed by reconstruction, structure identification and water content estimation.

3.1. Scattering correction and reconstruction

Since (heavy) water is a strong neutron scatterer, a scattering component is measured in addition to the direct transmitted neutrons. Without corrections this extra intensity would be misinterpreted as a too high transmission value or as an underestimation of the water content (θ) in the sample. The water content is defined as the volumetric fraction of the volume filled with water. A correction of the projection images was carried out prior to the sinogram generation. The correction essentially involved a deconvolution using the point-scattered function for water (Hassanein et al. [7]). The point spread function for water (here a mixture of D_2O and H_2O) was used since it was the strongest scatterer present in the scanned samples. The shape of the point-scattered function was determined using the gray value as starting point for a Monte Carlo simulation of the neutron scattering. The reconstruction of the corrected slices was made using a fast back projection algorithm (GridRec [8]) using a Shepp–Logan filter with the normed cut-off frequency $f_c = 0.5$ Hz/Hz. The resulting set of images are denoted as $I(x, y, z, t)$, where x, y, and z are the Cartesian coordinates and t is the time stamp of the time frame.

3.2. Structure identification

The aim of the experiment was to determine the water content per sand cube in the structure. A further step was to relate the water content to one of the two sand types. As an initial part of this task we had to identify the interface planes between all cubes in the arrangement.

Given a 3D image I that fulfills the requirement that it contains a structure built up by small cubes arranged in a rectilinear grid parallel to the principal axes. The sub-cube interfaces can be detected using the absolute gradient information of the smoothed original image,

$$I_\sigma = G_\sigma I \tag{1}$$

where G_σ is a 3D Gaussian convolution kernel with the variance σ^2. The smoothing was introduced to reduce the impact of gray level inhomogeneities originating from noise and structures others than the cube edges.

The interface planes for the cube arrangement were identified using projection profiles parallel to the principal axes of the image, given by

$$p_x(x) = \sum_y \sum_z |\nabla I_\sigma|(x, y, z) \tag{2}$$

$$p_y(y) = \sum_x \sum_z |\nabla I_\sigma|(x, y, z) \tag{3}$$

$$p_z(z) = \sum_x \sum_y |\nabla I_\sigma|(x, y, z) \tag{4}$$

These profiles are shown in Fig. 3.

From the gradient profiles p_x through p_z, the interface indicators were found using the morphological extended maximum operator, $\mathrm{EMAX}_h(f)$ [9]. This operator identifies regions in the signal f that have a local height larger than h. Each region corresponding to a local maximum with hight h generates a plateau for as shown in Fig. 4 and ensures that no local maxima other than the interface peaks are detected. The height h in the figure is exaggerated to illustrate the function of the operator. As we were interested in single points only for our purpose we selected the local maximum of the intervals indicated by each plateau as

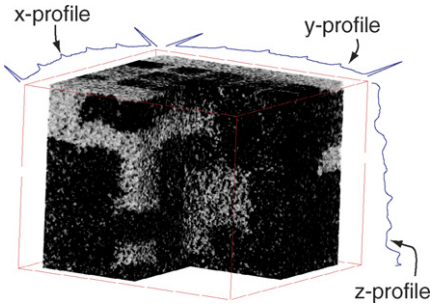

Fig. 3. Projected profiles from $|\nabla I_\sigma|$ plotted on the edges of the measured image I.

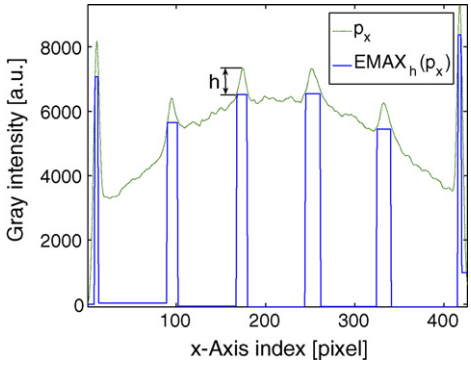

Fig. 4. The morphological EMAX_h-operator applied on a projection profile (p_x).

our interface point. Finally, center coordinates of each cube were computed as the half distance between two consequent interface points. The center coordinates will further on be denoted by the triplet $C_{ijk} = \{x, y, z\}$, were the indices i, j, and k refers to the position in the cube arrangement and x, y, and z are the midpoint positions of the indicated cube along each coordinate axis. The center coordinate variable will have the dimensions $5 \times 5 \times 6$ and it matches the indicator varible S_{material}.

3.3. Estimation of the local water content

From drainage experiments on the column in the laboratory we knew the water content in the sample for the initial state (wet) and also for the equilibrium state after drainage. By relating these measurements to the average of all voxels in the sand, we could deduce the absolute water content of the extracted sub-cubes in two steps. The average gray value of the sand voxels for the whole sample was computed as

$$A_{\text{sample}}(t) = \frac{1}{\text{Card}(I_{\text{sand}})} \sum_{\mathbf{q} \in I_{\text{sand}}} I(\mathbf{q}, \text{t}) \tag{5}$$

where $\mathbf{q}$ is a coordinate triplet $\{x, y, z\}$ within the image. The set of voxels that belong to the sand structure is denoted as I_{sand}. Card(g) is the cardinality of set g, i.e. the number of elements in the set. To avoid bias due to scattering on the edges near the container we used 80% of the sand volume as I_{sand} to compute the average gray level of the initial image $A_{\text{sample}}(0)$ and of the image at equilibrium $A_{\text{sample}}(t_{\text{eq}})$. The measured gray value (attenuation coefficient) has a linear relationship to the water and sand mass [10]. Hence, was the water content $\theta_{ijk}(t)$ of each cube computed as

$$\theta_{ijk}(t) = cA_{ijk}(t) + m \tag{6}$$

where c and m are constants determined using $A_{\text{sample}}(0)$ and $A_{\text{sample}}(t_{\text{eq}})$ from the images and measured values for the initial water content and the water content after equilibration. $A_{ijk}(t)$ is the average of the gray values in the cubes and was computed using box shaped regions (R_{ijk}) with side lengths U,V, and W centered around the previously chosen center points as

$$A_{ijk}(t) = \frac{1}{\text{Card}(R_{ijk})} \sum_{\mathbf{q} \in R_{ijk}} I(\mathbf{q}, t) \tag{7}$$

In our experiment we used $U = V = 41$ and $W = 29$ to reflect the deviation of the sand cube shape from a true cube. The metric dimensions of the box regions were 5.2 mm × 5.2 mm × 3.7 mm. The chosen window left some voxels margin to the identified interface planes. The margin was used since we wanted to avoid to introduce a bias due to transient flow behavior near the edges between two adjacent cubes. Fig. 5 shows a volume rendered example of data masked in the described way.

4. Results

The processed images resulted in two time series of reduced images with one water content estimate per sub-cube. To study and visualize the results we used the indicator variable (S_{material}) from the packing of the sample to relate the water content estimates to fine or coarse sand. Using this information we can visualize the accumulative properties of the fine sand and show how the coarse sand was drained faster.

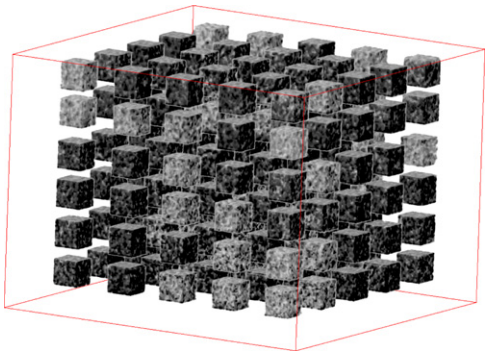

Fig. 5. The measured data masked by the identified box shaped regions. The average gray level intensity for each cube will be computed using these regions. Bright voxels represent dry sand.

To drain soil material, the applied suction force must overcome the pore-size dependent capillary forces. For the coarse material, suction values between 1000 and 1500 Pa must be applied to drain the pores. The applied suction must be doubled to drain the fine material. In course of the experiment suctions high enough to drain the coarse material were reached after 3 min. After 6 min, the suction was doubled and the fine material started to drain as well. The time delay between the drainage of the coarse and fine material can be seen in Figs. 6 and 7. Fig. 6 shows the water contents of the fine and coarse sands for the whole sample during drainage, while Fig. 7 visualizes the spatio-temporal water distribution per structure layer.

In case of the following wetting process was the maximum water content reached earlier for the fine material, Figs. 8 and 9 show this. This behavior can be explained by two effects. Firstly, the water content after the drainage process was higher in the

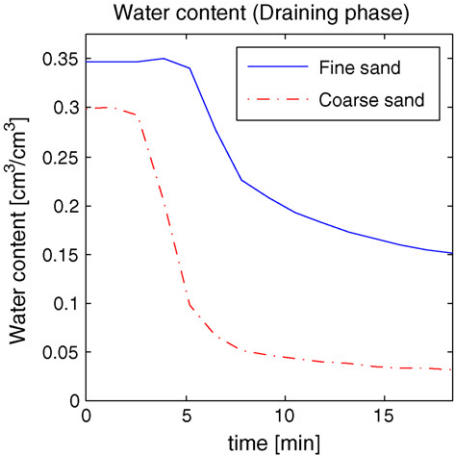

Fig. 6. Curves showing the water contents in the fine and coarse sand fractions during the draining phase.

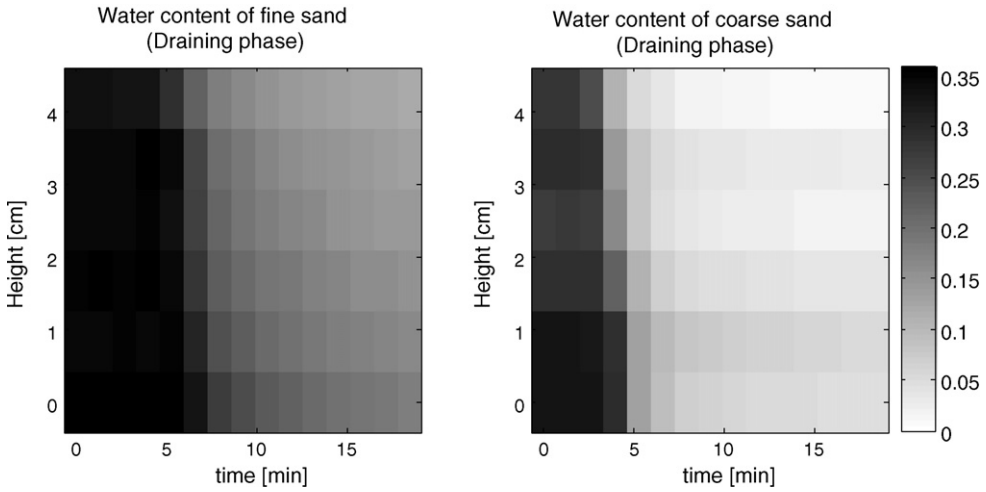

Fig. 7. The spatio-temporal distribution of the water content in the fine and coarse sands during the draining phase. The water content is represented by gray scales.

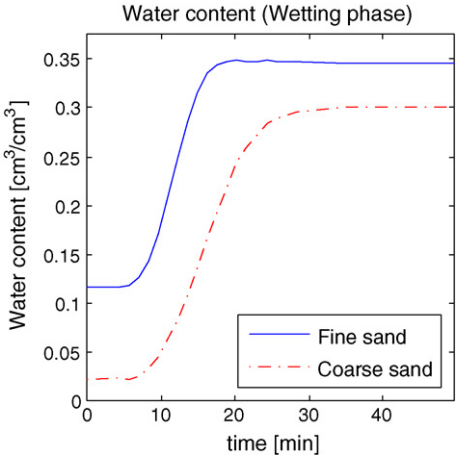

Fig. 8. Curves showing the water contents in the fine and coarse sand fractions during the rewetting phase.

fine material. Due to the higher water content, water flow was enhanced in the fine material and more water could enter the fine material than into the coarse sand. Secondly, by reducing the applied suction during the wetting experiment, more and more of the fine pores with high capillary forces were re-filled while the forces in the coarse material were too small to suck in the water.

Fig. 10 shows the 3D distribution of the water content in the coarse sand at different stages of the drainage phase of the experiment. The renderings in this figure show the average water content in the cubes at four times during the drainage. The images reflect the initial saturated condition, two intermediate steps during draining and finally the water content at the equilibrium state for the applied suction. In panel 10d can an isolated occurrence of water be observed in the upper part of the column. This locally slightly increased water content corresponds to a horizontal region with coarse sand that was weakly connected to the continuous region. Effects of this kind show the importance of structure on the hydraulic properties of the sample.

Finally we want to address the repeatability of our experiment by showing three repeated drainage sequences in Fig. 11 for the fine sand and Fig. 12 for the coarse sand. The curves representing the dynamic part of our experiment show a similar response in both fine and coarse sand over repeated experiments. The decreasing initial water content can be explained

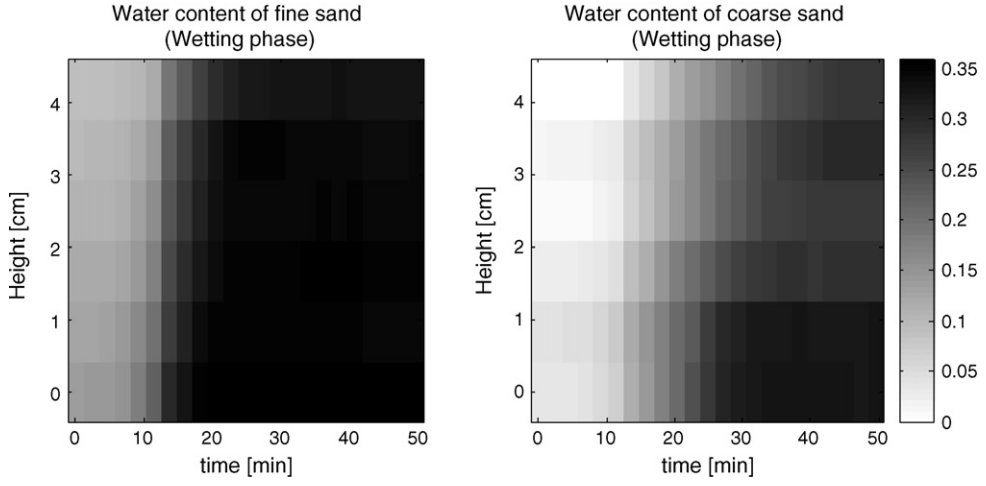

Fig. 9. The spatio-temporal distribution of the water content in the fine and coarse sands during the wetting phase. The water content is represented by gray scales.

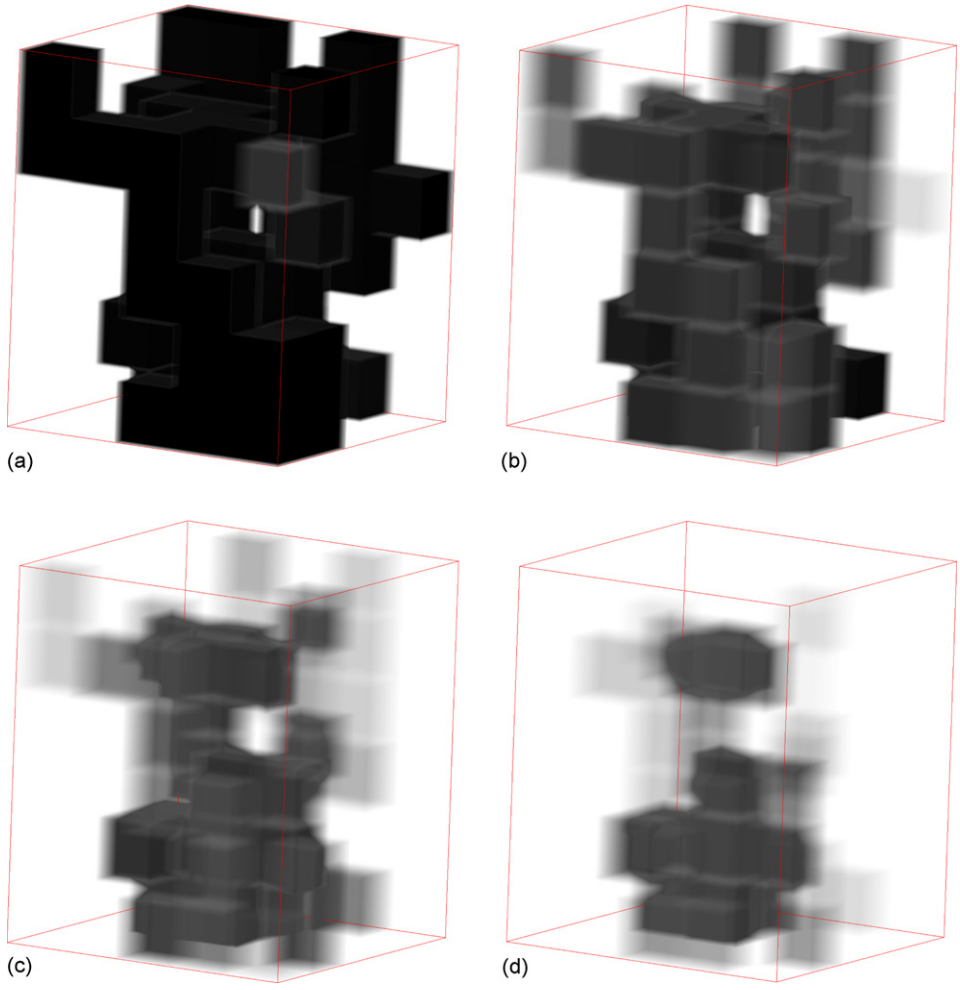

Fig. 10. Volume renderings of average water content at different times of the draining phase. Initial saturated condition (a), intermediate conditions (b) and (c), and water content at equilibrium for the applied suction force (d). Only the coarse sand fraction visualized and dark regions represent a higher water content.

by the inclusion of air bubbles during the wetting process. With each repeated drainage and wetting process, more air was enclosed. However, after a few more iterations, the initial water content would become constant. Unfortunately there was beam failure in the end of the second attempt. This is most visible in the fine sand curves. Ignoring the outlier produced by the beam failure, we claim that the repeatability of the experiment is good.

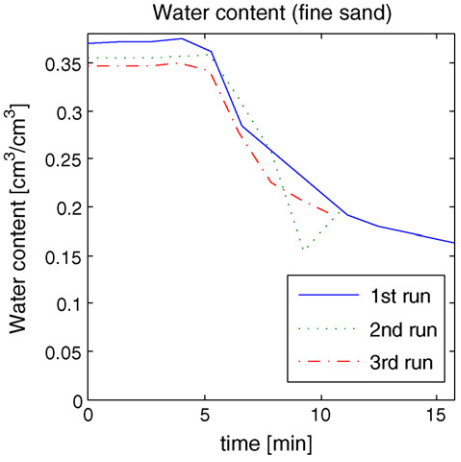

Fig. 11. Curves showing the water contents in the fine and coarse sand fractions during the draining phase.

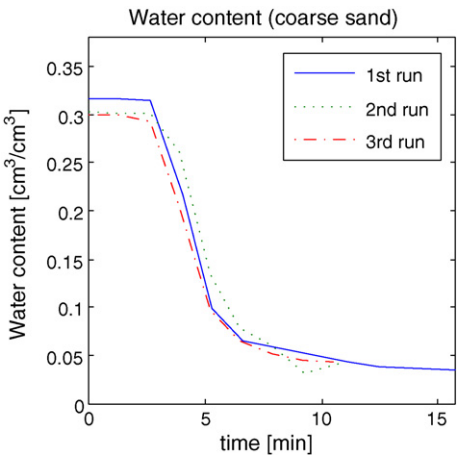

Fig. 12. Curves showing the water contents in the fine and coarse sand fractions during the rewetting phase.

5. Summary

Tomography using thermal neutrons as illuminating source gives us a tool to quantify, visualize, and study the water distribution in heterogeneous sand structures under water saturated and unsaturated conditions. The NEUTRA facility beamline at Paul Scherrer Institute, Switzerland, is capable of capturing the dynamics of our experiment with a sufficient time resolution to register the water content during drainage and wetting processes. We could verify that different soil materials are relevant for wetting and drainage processes respectively. The coarse sand is of most importance during the drainage phase, while during the rewetting phase the fine sand is rewetted faster than the coarse sand. We could furthermore show that the structure of fine and coarse sand has an impact the flow behavior.

References

[1] W. Jury, R. Horton, Soil Physics, 6th ed., John Wiley and Sons, 2004.
[2] D. Wildenschild, K. Jensen, Laboratory investigations of effective flow behavior in unsaturated heterogeneuos sands, Water Resour. Res. 35 (1) (1999) 17–27.
[3] P. Lehmann, F. Stauffer, C. Hinz, O. Dury, H. Flühler, Effect of hysteresis on water flow in a sand column with a fluctuating capillary fringe, J. Contam. Hydrol. 33 (1998) 81–100.
[4] B. Schultze, O. Ippisch, B. Huwe, W. Durner, Dynamic nonequilibrium during unsaturated water flow, in: M.T. van Genuchten, F.J. Leij, L. Wu (Eds.), Proceedings of the International Workshop on Characterization and Measurement of the Hydraulic Properties of Unsaturated Porous Media, University of California, Riverside, CA, 1999, pp. 877–892.
[5] N. Ursino, T. Gimmi, Combined effect of heterogeneity, anisotropy and saturation on steady state flow and transport: structure recognition and numerical simulation, Water Resour. Res. 40 (1) (2004) 1–18.
[6] E. Lehmann, P. Vontobel, L. Wiezel, Properties of the radiography facility NEUTRA at SINQ and it's potential for use as European reference facility, in: Proceedings of the Sixth World Conference on Neutron Radiography, 1999.
[7] R. Hassanein, E. Lehmann, P. Vontobel, Methods of scattering corrections for quantitative neutron radiography, Nucl. Instrum. Meth. Phys. Res. (A) 542 (1–3) (2005) 353–360.
[8] B.A. Dowd, G.H. Campbell, R.B. Marr, V. Nagarkar, S. Tipflis, L. Axe, D.P. Siddons, Developments in synchrotron X-ray computed microtomography at the National Synchrotron Light Source, in: Proceedings of the SPIE Conference on Developments in X-Ray Tomography II, vol. 3772, SPIE, 1999, pp. 224–236.
[9] P. Soille, Morphological Image Analysis, 2nd ed., Springer-Verlag, 2002.
[10] A. Kak, M. Slaney, Principles of Computerized Tomographic Imaging, IEEE Press, 1988.